Computers and Fluids 300 (2025) 106739

Contents lists available at ScienceDirect

Computers and Fluids

journal homepage: www.elsevier.com/locate/compfluid

# A time-dependent boundary-integral algorithm for nonlinear interfacial waves

Xin Guan [a,*], Jean-Marc Vanden-Broeck [b]

[a] Department of Mathematics, Imperial College London, London, SW7 2AZ, United Kingdom
[b] Department of Mathematics, University College London, London, WC1E 6BT, United Kingdom

ARTICLE INFO

*Keywords:*
Interfacial waves
Water waves
Boundary-integral equations
Numerical simulation

ABSTRACT

A boundary-integral algorithm based on an Eulerian or mixed Eulerian–Lagrangian description is presented for simulating two-dimensional unsteady nonlinear interfacial waves. It uses the tangent angle and the density-weighted velocity potential as primary unknowns, with the arclength used to parameterize the interface. Therefore, overhanging waves can be readily simulated. Cauchy's integral formula is used to solve Laplace's equation efficiently and accurately, for waves on deep water, finite-depth water or bottom topography. The numerical scheme is neutrally stable and conserves energy with superior accuracy. No significant numerical stiffness is observed, allowing for very long-term simulations of various physical scenarios.

## 1. Introduction

Waves at the interface of two immersible fluids are known as interfacial waves. As a generalized model of water waves, they can date back to Kelvin and Helmholtz in studies of hydrodynamic instabilities. Interfacial waves can model a variety of physical scenarios, including air–water interactions and oceanic internal waves. These processes are typically highly nonlinear and complex, often beyond the capabilities of weakly nonlinear models such as the Korteweg–de Vries equation and the nonlinear Schrödinger equation. In such cases, direct numerical simulation becomes the only viable approach.

Powerful numerical methods have been invented to simulate water waves for decades. With the assumptions that the fluid motion is incompressible, irrotational and inviscid, the governing Euler equations are simplified to the Laplace's equation with free boundary conditions at water surface. Therefore, boundary-integral algorithms are particularly attractive among numerical algorithms for water waves. In two dimensions, they can be primarily separated into three categories:

(1) Green's function method based on Green's identities [1–5].
(2) Cauchy's integral method based on Cauchy's integral formula [6–9].
(3) Vortex method based on dipole distributions and the Biot–Savart integral [9,10].

In addition, there are other numerical methods based on the conformal mapping technique [11] and the expansion of Dirichlet-to-Neumann (DtN) operator [12].

Using a Lagrangian parameter, the surface is discretized by a group of fluid markers. The physical coordinates of these markers are integrated in time and then provided to the boundary-integral equations to solve the velocity on the surface. This approach leads to a simple mathematical formulation, and is particularly efficient when studying breaking waves [1,7], for allowing Lagrangian makers to cluster in high-curvature region. In comparison, methods based on the Eulerian description need to fix the location of surface collocation points. This can be performed by fixing the $x$-coordinate [3,4] or the arclength [2] in physical space, or by fixing other parameters in certain transformed spaces [11,13]. The first approach has a restriction that the surface must be a graph of $x$. Therefore, it becomes invalid when waves overturn. The latter two approaches do not have this limitation, although their mathematical formulations is more complex.

When applying these numerical methods to inviscid interfacial waves, the velocity discontinuity across the interface naturally forms a vortex sheet, making vortex methods particularly popular. Most applications in this category focus on the motion of interfaces in unbounded regions, including wave propagation, the Rayleigh–Taylor (R–T) instability and the Kelvin–Helmholtz (K–H) instability [14–17]. Boundary-integral algorithms based on Cauchy's integral formula, although less commonly used, have advantages in handling waves over finite-depth water and bottom topography. A related work on water waves [9] examined the effects of bottom topography on gravity-capillary waves. For two-layer interfacial waves, Grue et al. [18] investigated the effects of bottom topography on unsteady transcritical

* Corresponding author.
*E-mail address:* xin.guan.20@ucl.ac.uk (X. Guan).

https://doi.org/10.1016/j.compfluid.2025.106739
Received 24 November 2024; Received in revised form 11 May 2025; Accepted 1 July 2025
Available online 10 July 2025

flows. This work extended the algorithm developed by Dold [6] for surface water waves, which was based on a Lagrangian framework.

In many situations, surface tension plays an important role on interfacial waves, either as a real physical effect or a regularization of the K-H instability. In this context, the Lagrangian approach may lead to an overly sparse distribution of sample particles, resulting in poor physical resolution. When studying the R–T instability, Baker et al. [14] found that the sample particles tend to move away from the developing spike and bubble regions, thus restricting the numerical accuracy significantly. In addition, accumulation of Lagrangian markers increases local wave number and may cause severe numerical stiffness, as reported by Hou et al. [16]. To address this issue, a strategy based on redistribution of sample points was used [19,20]. However, this may lead to a smoothing effect and affect the numerical accuracy. On the other hand, Yang [2] established a numerical scheme using the Eulerian description and the Green's function method when studying a fluid falling into vacuum. Hou et al. [16] applied a similar idea using the vortex-sheet method and a small-scale decomposition technique when studying interfacial flows with surface tension. Both authors used the tangent angle $\theta$ as an unknown and then constructed the surface or interface from integrations involving $\theta$.

In this paper, we present a boundary-integral algorithm for two-dimensional unsteady nonlinear interfacial waves. The basic idea is to parameterize the interface using arclength and apply the Cauchy's integral formula to solve the Laplace's equation. In most cases, this is completed by using an iterative solver such as the generalized minimal residual (GMRES) method. The normal velocity is then obtained and used to integrate $\theta$ and the density-weighted velocity potential $\overline{\varphi}$ in time. Once $\theta$ is updated in time, the new interface can be numerically calculated. It is worth noting that the well-known Hamiltonian formulation uses the interface elevation $\eta$ and the density-weighted velocity potential $\overline{\varphi}$ as canonical variables. The normal velocity is obtained through a truncated DtN operator in terms of $\eta$ [12]. Therefore, this approach is restricted to small or moderate-amplitude waves. By contrast, the Cauchy's integral formula finds the true DtN operator by solving the full Laplace's equation. This allows the simulations of highly nonlinear waves. The recent work by Ambrose et al. [9] also employed the $\theta - s$ approach and Cauchy's integral formula, though their focus was on surface water waves. Thus, our work extends their approach to two-layer interfacial waves. Using our method, we simulate various wave phenomena, including the travelling and head-on collision of interfacial gravity-capillary solitary waves, the R–T instability, breaking of surface gravity waves and waves passing over bottom topography. To the best of our knowledge, the simulations of interfacial gravity-capillary solitary waves are the first numerical experiments based the full Euler equations. In addition, our numerical scheme is neutrally stable and conserves energy with superior numerical accuracy. It is therefore stable for long-term simulations.

This paper is organized as follows: Section 2 describes the background mathematical formulation, nondimensionalization and dispersion relation of two-layer interfacial waves. Section 3 explains the arclength parameterization and the $\theta - s$ method for interfacial waves. Section 4 demonstrates how to use the Cauchy's integral formula to solve the Laplace's equation for waves bounded by flat solid walls and waves over bottom topography. Section 5 shows the numerical procedure of solving the boundary-integral equation, time-stepping scheme, numerical filter and estimation of the numerical accuracy. Section 6 describes the numerical tests, including the travelling of interfacial gravity-capillary waves of periodic and solitary types, head-on collision of interfacial gravity-capillary solitary waves, the R–T instability in unbounded and bounded regions, breaking of surface waves, and surface gravity solitary waves passing over bottom topography. Finally, Section 7 contains conclusions and perspectives.

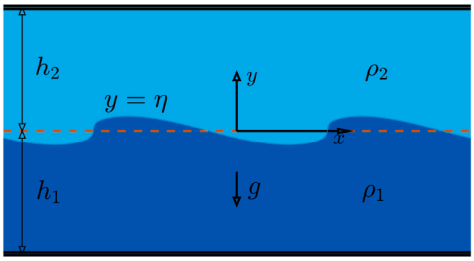


**Fig. 1.** A schematic of two-layer interfacial waves. The red dashed line denotes the mean water level. The black thick lines represent the top and bottom walls.

## 2. Mathematical formulation

### 2.1. Euler equations

We consider two-dimensional periodic interfacial waves between two immersible fluids (see Fig. 1). The densities and depths of each fluid are $\rho_i$ and $h_i$, where $i = 1$ and 2 represent the lower and upper fluids, respectively. Let $x$ and $y$ be the Cartesian coordinates in the horizontal and vertical directions. We let the $x$-axis align with the undisturbed interface. Assuming that the fluid motion is incompressible, irrotational and inviscid, we introduce the velocity potentials $\phi_1$ and $\phi_2$ for the lower and upper fluids. They satisfy the Laplace's equations

$$\phi_{1,xx} + \phi_{1,yy} = 0, \qquad -h_1 < y < \eta, \tag{1}$$

$$\phi_{2,xx} + \phi_{2,yy} = 0, \qquad \eta < y < h_2, \tag{2}$$

where the interface elevation $\eta(x,t)$ is periodic in $x$-direction with wave number $k$. At the interface, two kinematic boundary conditions and one dynamic boundary condition are imposed

$$\eta_t + \phi_{1,x}\eta_x - \phi_{1,y} = 0, \tag{3}$$

$$\eta_t + \phi_{2,x}\eta_x - \phi_{2,y} = 0, \tag{4}$$

$$\rho_1\phi_{1,t} - \rho_2\phi_{2,t} + \frac{\rho_1}{2}\left(\phi_{1,x}^2 + \phi_{1,y}^2\right) - \frac{\rho_2}{2}\left(\phi_{2,x}^2 + \phi_{2,y}^2\right) + (\rho_1 - \rho_2)g\eta - \frac{\sigma\eta_{xx}}{(1+\eta_x^2)^{3/2}} = 0, \tag{5}$$

where $g$ is the acceleration due to gravity, and $\sigma$ is the coefficient of surface tension. At the bottom and top boundaries, the impermeable conditions are satisfied. Here we consider two different scenarios.

1. Flat bottom: $h_1$ and $h_2$ are constants. The boundary conditions are

$$\phi_{1,y} = 0, \quad y = -h_1, \tag{6}$$

$$\phi_{2,y} = 0, \quad y = h_2. \tag{7}$$

2. Uneven bottom: $h_1(x)$ is a periodic function with wave number $k$, and $h_2$ is a constant. The boundary conditions become

$$\phi_{1,y} = -\phi_{1,x}h_{1,x}, \quad y = -h_1(x), \tag{8}$$

$$\phi_{2,y} = 0, \qquad y = h_2. \tag{9}$$

The primary goal of the paper is to provide a numerical algorithm to solve these equations and simulate the evolution of the interface, given appropriate initial conditions.

### 2.2. Nondimensonalization

Let the typical scalings of density, length, speed and time be $\rho_1$, $L$, $U$ and $T$. For different physical scenarios, we nondimensionalize the system according to the following choices:

1. $\sigma \neq 0$.

$$L = \left(\frac{\sigma}{\rho_1 g}\right)^{1/2}, \quad U = \left(\frac{\sigma g}{\rho_1}\right)^{1/4}, \quad T = \left(\frac{\sigma}{\rho_1 g^3}\right)^{1/4}. \tag{10}$$

2. $\sigma = 0$.

   (a) $h_1$ is finite.

$$L = \tilde{h}_1, \qquad U = \sqrt{g\tilde{h}_1}, \qquad T = \sqrt{\frac{\tilde{h}_1}{g}}, \tag{11}$$

   where $\tilde{h}_1$ is either $h_1$ in the flat-bottom case or an approximate mean depth in the uneven-bottom case.

   (b) $h_1$ is infinite.

$$L = \frac{1}{k}, \qquad U = \sqrt{\frac{g}{k}}, \qquad T = \sqrt{\frac{1}{gk}}. \tag{12}$$

### 2.3. Dispersion relation

We consider the flat-bottom case and search for solutions of the following travelling-wave form

$$\eta(x,t) = a_1 e^{i(kx-\omega t)} + c.c., \tag{13}$$

$$\phi_1(x,y,t) = a_2 \cosh(k(y+h_1)) e^{i(kx-\omega t)} + c.c., \tag{14}$$

$$\phi_2(x,y,t) = a_3 \cosh(k(y-h_2)) e^{i(kx-\omega t)} + c.c., \tag{15}$$

where $c.c.$ denotes complex conjugate, $\omega$ represents the angular frequency, and $a_1$ to $a_3$ are unknown constants. Note that the Laplace's Eqs. (1) and (2), and the impermeable conditions (6) and (7) are already satisfied. Assuming the amplitudes of $\eta$, $\phi_1$ and $\phi_2$ are small, we linearize the boundary conditions (3)–(5). By solving the coefficients $a_1$ to $a_3$, we obtain the dispersion relation

$$\omega^2 = \frac{(1-R)k + k^3}{\coth(kh_1) + R\coth(kh_2)}, \tag{16}$$

where $R = \rho_2/\rho_1$ is the density ratio. When $R < 1$, the right hand side of (16) is always non-negative, thus we have a linearly stable system. If we let $h_{1,2} \to \infty$, we obtain the dispersion relation of deep-water interfacial waves

$$\omega^2 = \frac{(1-R)|k| + |k|^3}{1+R}. \tag{17}$$

## 3. $\theta - s$ method

It is well-known that the motion of a two-dimensional interface

$$x = x(\alpha, t), \qquad y = \eta(\alpha, t), \tag{18}$$

where $\alpha$ labels the Lagrangian markers, is completely determined by its tangential velocity $\mathcal{T}$ and normal velocity $\mathcal{N}$. Introducing the tangent angle $\theta$ and the arclength $s$, we have the following $\theta - s$ equations [16]

$$\theta_t = \frac{\mathcal{N}_\alpha}{s_\alpha} + \frac{\theta_\alpha \mathcal{T}}{s_\alpha}, \tag{19}$$

$$s_{\alpha t} = \mathcal{T}_\alpha - \theta_\alpha \mathcal{N}, \tag{20}$$

which provide a Lagrangian description of the evolution of an interface. Note that Eqs. (19) and (20) are completely kinematic, thus are equivalent to the boundary conditions (3) and (4). However, a significant advantage of the $\theta - s$ approach is the ability to handle overhanging waves, i.e. when $\eta$ becomes a multivalued function of $x$. Using the following relation

$$\frac{\partial_\alpha}{s_\alpha} = \partial_s, \tag{21}$$

we can obtain an alternative formulation

$$\frac{D\theta}{Dt} = \mathcal{N}_s + \theta_s \mathcal{T}, \tag{22}$$

$$\frac{D\delta s}{Dt} = (\mathcal{T}_s - \theta_s \mathcal{N})\delta s, \tag{23}$$

where $D/Dt$ is the material derivative, and $\delta s$ denotes the arclength of an infinitesimal material element of the interface. Integrating (23) over a spatial period, we have

$$\frac{dS}{dt} = -\int_0^S \theta_s \mathcal{N}\, ds, \tag{24}$$

where the lower limit 0 is for convenience, and $S$ denotes the length of the interface in one period. Since our purpose is to establish a non-Lagrangian description, we introduce $l = s/S \in [0,1]$. The material derivative then becomes

$$\frac{D}{Dt} = \frac{\partial}{\partial t} + \frac{D}{Dt}\left(\frac{s}{S}\right)\frac{\partial}{\partial l}, \tag{25}$$

where

$$\frac{D}{Dt}\left(\frac{s}{S}\right) = \frac{1}{S}\frac{Ds}{Dt} + \frac{l}{S}\int_0^1 \theta_l \mathcal{N}\, dl. \tag{26}$$

Using (23), we have

$$\frac{Ds}{Dt} = \int_0^l (\mathcal{T}_l - \theta_l \mathcal{N})\, dl + \gamma(t). \tag{27}$$

Note that for inviscid interfacial waves, the tangential velocity is discontinuous across the interface, thus there is a freedom to choose $\mathcal{T}$. In the well-known vortex-sheet formulation, $\mathcal{T} = (\mathcal{T}_1 + \mathcal{T}_2)/2$. Grue et al. [18] chose a more general form $\mathcal{T} = \beta\mathcal{T}_1 + (1-\beta)\mathcal{T}_2$ with $0 \le \beta \le 1$. In principle, there is no preference among different choices in the Eulerian description as long as they are consistent with the definition of the material derivative (27). Without loss of generality, we let $\mathcal{T} = \mathcal{T}_1$ in the calculation. As a result, $Ds/Dt$ means the time derivative of the arclength corresponding to a specific Lagrangian marker of the lower fluid. The function $\gamma(t)$ reflects the fact that we can freely define the location where $s = 0$. In general, $\gamma(t)$ can be arbitrarily chosen, but there are two convenient choices of particular interest

(1) Case I: $\gamma = 0$. This means that the leftmost point in the computational domain is always the same Lagrangian marker for all time.

(2) Case II: $\gamma(t) = \mathcal{T}_1(0,t) - \mathcal{N}(0,t)\tan(\theta(0,t))$. One can show that this means that the leftmost point is precisely the Lagrangian marker located at the left boundary of a fixed physical domain. To see this, note that

$$u_1 = \frac{Dx(s,t)}{Dt} = x_s \frac{Ds}{Dt} + x_t, \tag{28}$$

where $u_1$ is the horizontal component of velocity. If we require $x(0,t) = \text{const.}$, then $x_t(0,t) = 0$. Using the identify $x_s = \cos\theta$ and substituting (27) into (28), we have

$$\begin{aligned}\gamma(t) &= \frac{u_1(0,t)}{\cos(\theta(0,t))} \\ &= \frac{\mathcal{T}_1(0,t)\cos(\theta(0,t)) - \mathcal{N}(0,t)\sin(\theta(0,t))}{\cos(\theta(0,t))}.\end{aligned} \tag{29}$$

Note that a potential drawback of the Case II setting is that it may break down when $\theta(0,t) = \pi/2$. Therefore, we prefer to use the Case I setting when dealing with overturned waves. Using (25) to (27), Eq. (22) becomes

$$\theta_t = \frac{\mathcal{T}_1(0,t)}{S}\theta_l + \frac{\mathcal{N}_l}{S} + \frac{\theta_l}{S}\int_0^l P(\theta_l \mathcal{N})\, dl - \frac{\gamma}{S}\theta_l, \tag{30}$$

where $P$ is the zero-mean operator defined as

$$P(f(l)) = f(l) - \int_0^1 f(l)\, dl. \tag{31}$$

The coordinates of interface can be calculated from the identity $z_l = Se^{i\theta}$, which gives

$$x = S\int_0^l \cos\theta\, dl + x_0(t), \tag{32}$$

$$\eta = S\int_0^l \sin\theta\,\mathrm{d}l + \eta_0(t). \tag{33}$$

The integral constants $x_0(t)$ and $\eta_0(t)$ are governed by

$$\frac{\mathrm{d}x_0}{\mathrm{d}t} = \begin{cases} \mathcal{T}_1(0,t)\cos\big(\theta(0,t)\big) - \mathcal{N}(0,t)\sin\big(\theta(0,t)\big), & \text{Case I} \\ 0, & \text{Case II} \end{cases} \tag{34}$$

$$\frac{\mathrm{d}\eta_0}{\mathrm{d}t} = \begin{cases} \mathcal{T}_1(0,t)\sin\big(\theta(0,t)\big) + \mathcal{N}(0,t)\cos\big(\theta(0,t)\big), & \text{Case I} \\ \mathcal{N}(0,t)/\cos\big(\theta(0,t)\big), & \text{Case II} \end{cases} \tag{35}$$

where the expressions for Case I are $u_1$ and $v_1$ (horizontal and vertical velocities) rewritten in terms of $\mathcal{T}_1$, $\mathcal{N}$ and $\theta$, and the expression in the second line of (35) is from the kinematic boundary condition

$$\eta_t = v_1 - u_1\eta_x = \mathcal{N}\sqrt{1+\eta_x^2} = \mathcal{N}/\cos\theta. \tag{36}$$

It is worth mentioning that the periodicity condition

$$S\int_0^1 \cos\theta\,\mathrm{d}l = \frac{2\pi}{k} \tag{37}$$

gives an extra constraint for $\theta$. Direct numerical integration of (32) may violate this constraint, as pointed by Hou et al. [16]. Their strategy is to consider the mean-zero projection of $\cos\theta$ only, i.e. they rewrote (32) as

$$x = \frac{2\pi}{k}l + S\int_0^l P\big(\cos\theta\big)\,\mathrm{d}l + x_0(t). \tag{38}$$

Ambrose et al. [9] used another strategy by considering the mean-zero projection of $\theta$ only. Interested readers are referred to their paper for details. Here we apply the strategy used by Hou et al. [16].

To rewrite the dynamic boundary condition (5), we introduce a density-weighted potential function $\overline{\varphi}$

$$\begin{aligned}\overline{\varphi}(l,t) &= \varphi_1(l,t) - R\varphi_2(l,t) \\ &= \phi_1\big(x(l,t),\eta(l,t),t\big) - R\phi_2\big(x(l,t),\eta(l,t),t\big).\end{aligned} \tag{39}$$

Taking the $s$-derivative, we obtain a density-weighted tangential velocity $\overline{\mathcal{T}}$

$$\overline{\mathcal{T}} = \overline{\varphi}_l/S = \mathcal{T}_1 - R\mathcal{T}_2. \tag{40}$$

When $R = 1$, $\overline{\mathcal{T}}$ becomes the well-known vortex-sheet strength. It can be shown that the dynamic boundary condition (5) becomes

$$\begin{aligned}\overline{\varphi}_t = \mathcal{T}_1(0,t)\overline{\mathcal{T}} + \frac{(1-R)\mathcal{N}^2}{2} - \frac{\mathcal{T}_1^2 - R\mathcal{T}_2^2}{2} - (1-R)\eta \\ + \frac{\theta_l}{S} + \overline{\mathcal{T}}\int_0^l P\big(\theta_l\mathcal{N}\big)\,\mathrm{d}l - \overline{\mathcal{T}}\gamma.\end{aligned} \tag{41}$$

A detailed derivation is shown in Appendix. Eqs. (24), (30), (34), (35) and (41) are the time-evolution equations of $S$, $\theta$, $x_0$, $\eta_0$ and $\overline{\varphi}$. To close the system, we still need to provide the normal velocity $\mathcal{N}$ which can be calculated from the Cauchy's integral formula.

## 4. Cauchy's integral formula

We introduce a complex variable $\zeta$

$$\zeta = \mathrm{e}^{-\mathrm{i}kz}, \tag{42}$$

where $z = x + \mathrm{i}y$. The transformation maps a periodic region in the physical plane to an annular region with wiggly boundaries in the $\zeta$-plane. Since the complex velocity $w_i = u_i - \mathrm{i}v_i$ is an analytic function of $z$, thus also of $\zeta$, it satisfies the Cauchy's integral formula

$$w_i(\zeta_0) = \frac{1}{\mathrm{i}\pi}\mathrm{p.v.}\oint_{C_i}\frac{w_i(\zeta)}{\zeta-\zeta_0}\,\mathrm{d}\zeta, \tag{43}$$

where p.v. denotes the Cauchy principal value, $C_i$ denotes the boundaries of the lower ($i = 1$) and upper ($i = 2$) fluids in the $\zeta$-plane, $\zeta_0$ is a point on the boundaries, and the dependence on time $t$ has been dropped for simplicity. Here we consider the cases when the bottom wall is either flat or uneven.

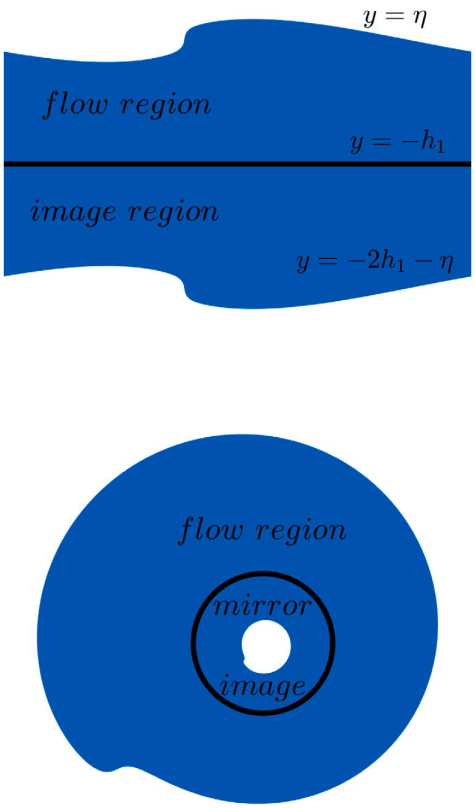


**Fig. 2.** Region of the lower fluid and its mirror image in the physical plane (top) and the $\zeta$-plane (bottom). The black curves correspond to the bottom wall and its image.

### 4.1. Flat bottom

Note that the complex velocity $w_i$ can be written as

$$w_i = (\mathcal{T}_i - \mathrm{i}\mathcal{N})\mathrm{e}^{-\mathrm{i}\theta}. \tag{44}$$

Substituting (44) into the Cauchy's integral formula (43) and using the Schwarz reflection principle (see Fig. 2 for an illustration for the lower fluid), we can obtain the boundary-integral equations for the lower layer and the upper layer

$$\begin{aligned}&\Big(\mathcal{T}_1(l_0) - \mathrm{i}\mathcal{N}(l_0)\Big)\mathrm{e}^{-\mathrm{i}\theta(l_0)} \\ &\quad = \frac{kS}{\pi}\int_0^1\left[\frac{\mathcal{T}_1(l) - \mathrm{i}\mathcal{N}(l)}{1-\zeta(l_0)/\zeta(l)} - \frac{\mathcal{T}_1(l) + \mathrm{i}\mathcal{N}(l)}{1-\zeta(l_0)/\zeta_{I1}(l)}\right]\mathrm{d}l,\end{aligned} \tag{45}$$

$$\begin{aligned}&\Big(\mathcal{T}_2(l_0) - \mathrm{i}\mathcal{N}(l_0)\Big)\mathrm{e}^{-\mathrm{i}\theta(l_0)} \\ &\quad = \frac{kS}{\pi}\int_0^1\left[\frac{\mathcal{T}_2(l) + \mathrm{i}\mathcal{N}(l)}{1-\zeta(l_0)/\zeta_{I2}(l)} - \frac{\mathcal{T}_2(l) - \mathrm{i}\mathcal{N}(l)}{1-\zeta(l_0)/\zeta(l)}\right]\mathrm{d}l,\end{aligned} \tag{46}$$

where $\zeta_{I1}$ and $\zeta_{I2}$ denote the images of the reflection of the interface with respect to the lower wall and the upper wall. The integrals are again in the sense of Cauchy's principal value, but we drop the p.v. in the following equations. Separating the real and imaginary parts, we have four real-valued boundary-integral equations

$$\mathcal{N}(l_0) = \int_0^1\Big(\mathcal{A}-\mathcal{B}\Big)\mathcal{T}_1(l)\,\mathrm{d}l + \int_0^1\Big(\mathcal{C}+\mathcal{D}\Big)\mathcal{N}(l)\,\mathrm{d}l, \tag{47}$$

$$\mathcal{N}(l_0) = \int_0^1\Big(\mathcal{B}-\mathcal{E}\Big)\mathcal{T}_2(l)\,\mathrm{d}l - \int_0^1\Big(\mathcal{D}+\mathcal{F}\Big)\mathcal{N}(l)\,\mathrm{d}l, \tag{48}$$

$$\mathcal{T}_1(l_0) = \int_0^1\Big(\mathcal{D}-\mathcal{C}\Big)\mathcal{T}_1(l)\,\mathrm{d}l + \int_0^1\Big(\mathcal{A}+\mathcal{B}\Big)\mathcal{N}(l)\,\mathrm{d}l, \tag{49}$$

$$\mathcal{T}_2(l_0) = \int_0^1 \Big(\mathcal{F} - \mathcal{D}\Big)\mathcal{T}_2(l)\,\mathrm{d}l - \int_0^1 \Big(\mathcal{B} + \mathcal{E}\Big)\mathcal{N}(l)\,\mathrm{d}l, \tag{50}$$

where $\mathcal{A}$ to $\mathcal{F}$ are

$$\mathcal{A} = \frac{kS}{\pi}\mathrm{Im}\left(\frac{\mathrm{e}^{\mathrm{i}\theta(l_0)}\mathrm{e}^{-2kh_1}/\zeta^*(l)}{\mathrm{e}^{-2kh_1}/\zeta^*(l) - \zeta(l_0)}\right), \quad \mathcal{B} = \frac{kS}{\pi}\mathrm{Im}\left(\frac{\mathrm{e}^{\mathrm{i}\theta(l_0)}}{1-\zeta(l_0)/\zeta(l)}\right),$$

$$\mathcal{C} = \frac{kS}{\pi}\mathrm{Re}\left(\frac{\mathrm{e}^{\mathrm{i}\theta(l_0)}\mathrm{e}^{-2kh_1}/\zeta^*(l)}{\mathrm{e}^{-2kh_1}/\zeta^*(l) - \zeta(l_0)}\right), \quad \mathcal{D} = \frac{kS}{\pi}\mathrm{Re}\left(\frac{\mathrm{e}^{\mathrm{i}\theta(l_0)}}{1-\zeta(l_0)/\zeta(l)}\right),$$

$$\mathcal{E} = \frac{kS}{\pi}\mathrm{Im}\left(\frac{\mathrm{e}^{\mathrm{i}\theta(l_0)}/\zeta^*(l)}{1/\zeta^*(l) - \zeta(l_0)/\mathrm{e}^{2kh_2}}\right),$$

$$\mathcal{F} = \frac{kS}{\pi}\mathrm{Re}\left(\frac{\mathrm{e}^{\mathrm{i}\theta(l_0)}/\zeta^*(l)}{1/\zeta^*(l) - \zeta(l_0)/\mathrm{e}^{2kh_2}}\right),$$

where Re and Im denote the real and imaginary parts, and $\zeta^*$ is the complex conjugate of $\zeta$. Note that when $h_1 \to \infty$, $\mathcal{A}$ and $\mathcal{C}$ vanish. This is what we expect since the bottom wall goes to infinity, thus the mirror image of the interface with respect to the bottom wall has zero contribution to the integral equations. However, when $h_2 \to \infty$, $\mathcal{E}$ and $\mathcal{F}$ do not vanish, but converges to the imaginary and real parts of $kS\mathrm{e}^{\mathrm{i}\theta(l_0)}/\pi$. Therefore, the imaginary and real parts of this term must have zero contribution to the integral equations and can be subtracted from $\mathcal{E}$ and $\mathcal{F}$. This was first pointed out in [6]. Therefore, $\mathcal{E}$ and $\mathcal{F}$ can be written as

$$\mathcal{E} = \frac{kS}{\pi}\mathrm{Im}\left(\frac{\mathrm{e}^{\mathrm{i}\theta(l_0)}\zeta(l)/\mathrm{e}^{2kh_2}}{1/\zeta^*(l) - \zeta(l_0)/\mathrm{e}^{2kh_2}}\right), \tag{51}$$

$$\mathcal{F} = \frac{kS}{\pi}\mathrm{Re}\left(\frac{\mathrm{e}^{\mathrm{i}\theta(l_0)}\zeta(l)/\mathrm{e}^{2kh_2}}{1/\zeta^*(l) - \zeta(l_0)/\mathrm{e}^{2kh_2}}\right). \tag{52}$$

Note that for given $\overline{\mathcal{T}}$ and $z$, Eqs. (47)–(50) only contain two independent unknowns, i.e. $\mathcal{N}$ and one of $\mathcal{T}_i\,(i = 1, 2)$. For convenience, we introduce a new function $\mathcal{U} = \mathcal{T}_1 + \mathcal{T}_2$. Then $\mathcal{T}_1$ and $\mathcal{T}_2$ can be expressed as

$$\mathcal{T}_1 = \frac{\overline{\mathcal{T}} + R\mathcal{U}}{1+R}, \qquad \mathcal{T}_2 = \frac{\mathcal{U} - \overline{\mathcal{T}}}{1+R}. \tag{53}$$

Multiplying (48) by $R$ and adding it to (47), we have

$$\mathcal{N}(l_0) = \int_0^1 \frac{\mathcal{C} + (1-R)\mathcal{D} - R\mathcal{F}}{1+R}\mathcal{N}(l)\,\mathrm{d}l + \int_0^1 \frac{R(\mathcal{A}-\mathcal{E})}{(1+R)^2}\mathcal{U}(l)\,\mathrm{d}l + \int_0^1 \left(\frac{\mathcal{A}+R\mathcal{E}}{(1+R)^2} - \frac{\mathcal{B}}{1+R}\right)\overline{\mathcal{T}}(l)\,\mathrm{d}l. \tag{54}$$

Adding (49) to (50), we have

$$\mathcal{U}(l_0) = \int_0^1 \Big(\mathcal{A} - \mathcal{E}\Big)\mathcal{N}(l)\,\mathrm{d}l + \int_0^1 \frac{\mathcal{F} - R\mathcal{C} - (1-R)\mathcal{D}}{1+R}\mathcal{U}(l)\,\mathrm{d}l + \int_0^1 \frac{2\mathcal{D} - \mathcal{C} - \mathcal{F}}{1+R}\overline{\mathcal{T}}(l)\,\mathrm{d}l. \tag{55}$$

These are two coupled Fredholm integral equations of the second kind for $\mathcal{N}$ and $\mathcal{U}$. Note that when $l \to l_0$,

$$\frac{\mathrm{e}^{\mathrm{i}\theta(l_0)}}{1-\zeta(l_0)/\zeta(l)} = \frac{\mathrm{i}}{kS(l-l_0)} + \frac{\mathrm{e}^{\mathrm{i}\theta(l_0)}}{2} + \frac{\theta_l(l_0)}{2kS} + O(l-l_0), \tag{56}$$

thus the function $\mathcal{D}$ is continuous at $l = l_0$. The singular integrals involving $\mathcal{B}$ can be calculated by noticing

$$\int_0^1 \mathcal{B}f(l)\,\mathrm{d}l = \int_{l_0-1/2}^{l_0+1/2}\left(\mathcal{B}f(l) - \frac{f(l_0)}{\pi(l-l_0)}\right)\mathrm{d}l + \frac{f(l_0)}{\pi}\int_{l_0-1/2}^{l_0+1/2}\frac{\mathrm{d}l}{l-l_0}, \tag{57}$$

where the last integral is identically zero, and the change of upper and lower limits is due to the periodicity property. The integrand inside the bracket becomes regular since

$$\mathcal{B}f(l) - \frac{f(l_0)}{\pi(l-l_0)} = \frac{f_l(l_0)}{\pi} + \frac{kSf(l_0)\sin\big(\theta(l_0)\big)}{2\pi} + O(l-l_0), \tag{58}$$

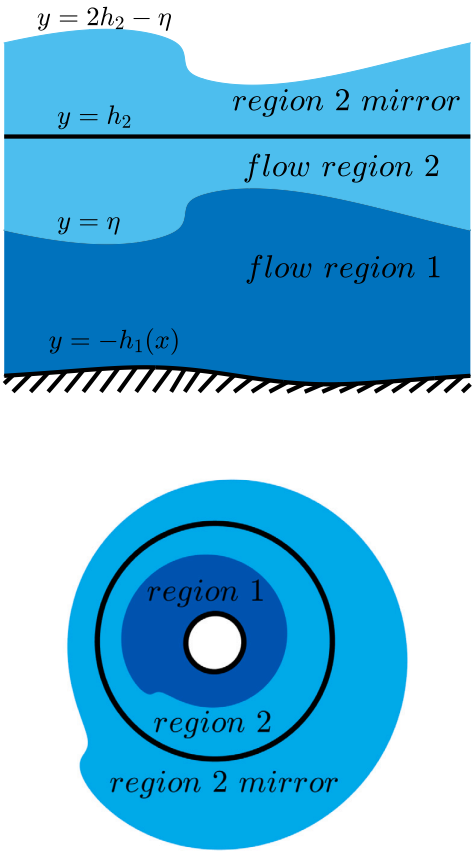


**Fig. 3.** Schematic of interfacial waves with a periodic bottom topography $h_1(x)$ in the physical region (top) and its image in the $\zeta$-plane (bottom). The top wall is assumed flat, thus the Schwarz reflection principle is used for the upper fluid in the Cauchy's integral formula. The small and large black curves correspond to the images of the upper and bottom walls.

provided $f(l)$ is smooth. There are two degenerate cases that are of particular interest:

- Surface waves ($R = 0$). Eq. (54) reduces to (47), which is used to solve $\mathcal{N}$ given $\mathcal{T}_1$ and $\theta$.
- Deep-water waves ($h_{1,2} \to \infty$). Functions $\mathcal{A}$, $\mathcal{C}$, $\mathcal{E}$, and $\mathcal{F}$ all vanish, and the integral Eqs. (54) and (55) are decoupled.

### 4.2. Uneven bottom

For a steady periodic bottom topography $y = -h_1(x)$, we introduce the complex variable $\zeta_b = \mathrm{e}^{-\mathrm{i}k(x-\mathrm{i}h_1(x))}$, the tangent angle $\theta_b = \tan^{-1}(-h_1'(x))$ and the tangent velocity $\mathcal{T}_b$ at the bottom. Here we assume that the topography has the same spatial period as the interfacial waves. In the $\zeta$-plane (see Fig. 3), we apply the Cauchy's integral formula. Since the normal velocity at the bottom is zero due to the impermeable condition, the Cauchy's integral formula for the lower fluid becomes

$$\Big(\mathcal{T}_1(l_0) - \mathrm{i}\mathcal{N}(l_0)\Big)\mathrm{e}^{-\mathrm{i}\theta(l_0)} = \frac{k}{\pi}\int_0^1 \left[\frac{S\big(\mathcal{T}_1(l) - \mathrm{i}\mathcal{N}(l)\big)}{1-\zeta(l_0)/\zeta(l)}\,\mathrm{d}l - \frac{S_b\mathcal{T}_b(l)}{1-\zeta(l_0)/\zeta_b(l)}\right]\mathrm{d}l, \tag{59}$$

$$\mathcal{T}_b(l_0)\mathrm{e}^{-\mathrm{i}\theta_b(l_0)} = \frac{k}{\pi}\int_0^1 \left[\frac{S\big(\mathcal{T}_1(l) - \mathrm{i}\mathcal{N}(l)\big)}{1-\zeta_b(l_0)/\zeta(l)}\,\mathrm{d}l - \frac{S_b\mathcal{T}_b(l)}{1-\zeta_b(l_0)/\zeta_b(l)}\right]\mathrm{d}l, \tag{60}$$

where the integrals go along the interface and the bottom wall (Schwarz reflection principle is not available for the lower layer), and $S_b$ is the length of the bottom topography in one spatial period. Separating the real and imaginary parts, we have five real-valued integral equations

$$\mathcal{N}(l_0) = \int_0^1 \mathcal{D}\mathcal{N}(l)\,\mathrm{d}l - \int_0^1 \mathcal{B}\mathcal{T}_1(l)\,\mathrm{d}l + \int_0^1 \mathcal{G}\mathcal{T}_b(l)\,\mathrm{d}l, \tag{61}$$

$$\mathcal{N}(l_0) = \int_0^1 \Big(\mathcal{B}-\mathcal{E}\Big)\mathcal{T}_2(l)\,\mathrm{d}l - \int_0^1 \Big(\mathcal{D}+\mathcal{F}\Big)\mathcal{N}(l)\,\mathrm{d}l, \tag{62}$$

$$\mathcal{T}_1(l_0) = \int_0^1 \mathcal{D}\mathcal{T}_1(l)\,\mathrm{d}l + \int_0^1 \mathcal{B}\mathcal{N}(l)\,\mathrm{d}l - \int_0^1 \mathcal{I}\mathcal{T}_b(l)\,\mathrm{d}l, \tag{63}$$

$$\mathcal{T}_2(l_0) = \int_0^1 \Big(\mathcal{F}-\mathcal{D}\Big)\mathcal{T}_2(l)\,\mathrm{d}l - \int_0^1 \Big(\mathcal{B}+\mathcal{E}\Big)\mathcal{N}(l)\,\mathrm{d}l, \tag{64}$$

$$\mathcal{T}_b(l_0) = \int_0^1 \mathcal{J}\mathcal{T}_1(l)\,\mathrm{d}l + \int_0^1 \mathcal{K}\mathcal{N}(l)\,\mathrm{d}l - \int_0^1 \mathcal{L}\mathcal{T}_b(l)\,\mathrm{d}l, \tag{65}$$

where $\mathcal{G}$ to $\mathcal{L}$ are

$$\mathcal{G} = \frac{kS_b}{\pi}\mathrm{Im}\left(\frac{\mathrm{e}^{\mathrm{i}\theta(l_0)}\zeta_b(l)}{\zeta_b(l)-\zeta(l_0)}\right), \quad \mathcal{I} = \frac{kS_b}{\pi}\mathrm{Re}\left(\frac{\mathrm{e}^{\mathrm{i}\theta(l_0)}\zeta_b(l)}{\zeta_b(l)-\zeta(l_0)}\right),$$

$$\mathcal{J} = \frac{kS}{\pi}\mathrm{Re}\left(\frac{\mathrm{e}^{\mathrm{i}\theta_b(l_0)}\zeta(l)}{\zeta(l)-\zeta_b(l_0)}\right), \quad \mathcal{K} = \frac{kS}{\pi}\mathrm{Im}\left(\frac{\mathrm{e}^{\mathrm{i}\theta_b(l_0)}\zeta(l)}{\zeta(l)-\zeta_b(l_0)}\right),$$

$$\mathcal{L} = \frac{kS_b}{\pi}\mathrm{Re}\left(\frac{\mathrm{e}^{\mathrm{i}\theta_b(l_0)}\zeta_b(l)}{\zeta_b(l)-\zeta_b(l_0)}\right).$$

When $l \to l_0$, we have

$$\frac{\mathrm{e}^{\mathrm{i}\theta_b(l_0)}}{1-\zeta_b(l_0)/\zeta_b(l)} = \frac{\mathrm{i}}{kS_b(l-l_0)} + \frac{\mathrm{e}^{\mathrm{i}\theta_b(l_0)}}{2} + \frac{\theta_{b,l}(l_0)}{2kS_b} + O(l-l_0), \tag{66}$$

thus $\mathcal{L}$ is continuous at $l = l_0$. Rewriting these equations by using the variables $\overline{\mathcal{T}}$, $\mathcal{U}$ and $\mathcal{T}_b$, we obtain three coupled real-valued boundary-integral equations

$$\begin{aligned}\mathcal{N}(l_0) = {} & \int_0^1 \frac{(1-R)\mathcal{D}-R\mathcal{F}}{1+R}\mathcal{N}(l)\,\mathrm{d}l - \int_0^1 \frac{\mathcal{E}}{(1+R)^2}\mathcal{U}(l)\,\mathrm{d}l \\ & + \int_0^1 \frac{\mathcal{G}}{1+R}\mathcal{T}_b(l)\,\mathrm{d}l + \int_0^1 \frac{\mathcal{E}-(1+R)\mathcal{B}}{(1+R)^2}\overline{\mathcal{T}}(l)\,\mathrm{d}l,\end{aligned} \tag{67}$$

$$\begin{aligned}\mathcal{U}(l_0) = {} & \int_0^1 \frac{\mathcal{F}-(1-R)\mathcal{D}}{1+R}\mathcal{U}(l)\,\mathrm{d}l - \int_0^1 \mathcal{E}\mathcal{N}(l)\,\mathrm{d}l \\ & - \int_0^1 \mathcal{I}\mathcal{T}_b(l)\,\mathrm{d}l + \int_0^1 \frac{2\mathcal{D}-\mathcal{F}}{1+R}\overline{\mathcal{T}}(l)\,\mathrm{d}l,\end{aligned} \tag{68}$$

$$\begin{aligned}\mathcal{T}_b(l_0) = {} & \int_0^1 \mathcal{K}\mathcal{N}(l)\,\mathrm{d}l + \int_0^1 \frac{R\mathcal{J}}{1+R}\mathcal{U}(l)\,\mathrm{d}l - \int_0^1 \mathcal{L}\mathcal{T}_b(l)\,\mathrm{d}l \\ & + \int_0^1 \frac{\mathcal{J}}{1+R}\overline{\mathcal{T}}(l)\,\mathrm{d}l.\end{aligned} \tag{69}$$

Note that Grue et al. [18] used a similar approach and obtained a formulation different from ours, because they applied the Cauchy's integral formula in the physical space.

For surface waves over bottom topography ($R = 0$), the formulation can be simplified to the following two integral equations for $\mathcal{N}$ and $\mathcal{T}_b$

$$\mathcal{N}(l_0) = \int_0^1 \mathcal{D}\mathcal{N}(l)\,\mathrm{d}l + \int_0^1 \mathcal{G}\mathcal{T}_b(l)\,\mathrm{d}l - \int_0^1 \mathcal{B}\mathcal{T}_1(l)\,\mathrm{d}l, \tag{70}$$

$$\mathcal{T}_b(l_0) = \int_0^1 \mathcal{K}\mathcal{N}(l)\,\mathrm{d}l - \int_0^1 \mathcal{L}\mathcal{T}_b(l)\,\mathrm{d}l + \int_0^1 \mathcal{J}\mathcal{T}_1(l)\,\mathrm{d}l. \tag{71}$$

## 5. Numerical algorithm

We discretize the interface/topography by $N$ equally spaced collocation points of $l$

$$l_m = \frac{m-1}{N}, \qquad m = 1, 2\cdots, N. \tag{72}$$

In principle, the number of grid points on the interface and bottom topography can be different. All spatial-derivatives with respect to $l$ are calculated by using the fast Fourier transform. Note that the Case I choice (see the explanation above (28)) then corresponds to a mixed Eulerian–Lagrangian description in the sense that the leftmost collocation point is a Lagrangian marker of the lower fluid, while other points are not Lagrangian markers but equally spaced grid points in arclength. In this sense, the Case II choice corresponds to an Eulerian description.

### 5.1. Solving boundary-integral equations

All boundary integrals are calculated by using the trapezoid rule, which gives spectral accuracy for periodic functions. Eqs. (54) and (55) are rewritten into a more compact form

$$\begin{aligned}&\begin{pmatrix} I - \frac{C-R\mathcal{F}+(1-R)\mathcal{D}}{1+R}\Delta l & \frac{R(\mathcal{E}-\mathcal{A})}{(1+R)^2}\Delta l \\ (\mathcal{E}-\mathcal{A})\Delta l & I - \frac{\mathcal{F}-R\mathcal{C}-(1-R)\mathcal{D}}{1+R}\Delta l \end{pmatrix}\cdot\begin{pmatrix}\mathcal{N}\\ \mathcal{U}\end{pmatrix} \\ &= \begin{pmatrix} \frac{\mathcal{A}+R\mathcal{E}}{(1+R)^2}\cdot\overline{\mathcal{T}} - \frac{\mathcal{B}}{1+R}\cdot\overline{\mathcal{T}} - \frac{\partial\overline{\mathcal{T}}/\partial l}{\pi(1+R)} \\ \frac{2\mathcal{D}-\mathcal{C}-\mathcal{F}}{1+R}\cdot\overline{\mathcal{T}} \end{pmatrix}\Delta l,\end{aligned} \tag{73}$$

where $I$ denotes the identity matrix. For the uneven-bottom case, Eqs. (67)–(69) become

$$\begin{aligned}&\begin{pmatrix} I - \frac{(1-R)\mathcal{D}-R\mathcal{F}}{1+R}\Delta l & \frac{\mathcal{E}}{(1+R)^2}\Delta l & -\frac{\mathcal{G}}{1+R}\Delta l \\ \mathcal{E}\Delta l & I - \frac{\mathcal{F}-(1-R)\mathcal{D}}{1+R}\Delta l & \mathcal{I}\Delta l \\ -\mathcal{K}\Delta l & -\frac{R\mathcal{J}}{1+R}\Delta l & I + \mathcal{L}\Delta l \end{pmatrix}\cdot\begin{pmatrix}\mathcal{N}\\ \mathcal{U}\\ \mathcal{T}_b\end{pmatrix} \\ &= \begin{pmatrix} \frac{\mathcal{E}-(1+R)\mathcal{B}}{(1+R)^2}\cdot\overline{\mathcal{T}} - \frac{\partial\overline{\mathcal{T}}/\partial l}{\pi(1+R)} \\ \frac{2\mathcal{D}-\mathcal{F}}{1+R}\cdot\overline{\mathcal{T}} \\ \frac{\mathcal{J}}{1+R}\overline{\mathcal{T}} \end{pmatrix}\Delta l.\end{aligned} \tag{74}$$

Note that on the right-hand side, $\mathcal{B}\cdot\overline{\mathcal{T}}$ represents

$$\sum_{n=1,n\neq m}^{N} \mathcal{B}(l_m, l_n)\overline{\mathcal{T}}(l_n) + \frac{k\overline{\mathcal{T}}(l_m)\sin\big(\theta(l_m)\big)}{2\pi}. \tag{75}$$

For surface waves over bottom topography, Eqs. (70) and (71) become

$$\begin{pmatrix} I - \mathcal{D}\Delta l & -\mathcal{G}\Delta l \\ -\mathcal{K}\Delta l & I + \mathcal{L}\Delta l \end{pmatrix}\cdot\begin{pmatrix}\mathcal{N}\\ \mathcal{T}_b\end{pmatrix} = \begin{pmatrix} -\mathcal{B}\cdot\mathcal{T}_1 - \frac{\partial\mathcal{T}_1/\partial l}{\pi} \\ \mathcal{J}\cdot\mathcal{T}_1 \end{pmatrix}\Delta l, \tag{76}$$

where $\mathcal{B}\cdot\mathcal{T}_1$ follows (75) similarly. Eqs (73) can be solved efficiently by using the GMRES iterative solver. In most cases, it takes only 2 or 3 iterations to reduce the residuals to $10^{-12}$, which is chosen as the threshold of convergence. On the other hand, Eqs. (74) and (76) are solved by using linear solvers based on Gaussian elimination. It turns out that the coefficient matrices of these two equations, although having rather small condition number, possess dispersive eigenvalues, due to the off-diagonal blocks. Thus preconditioning is essential for the GMRES method to work well. We have used the coefficient matrices with all diagonal blocks replaced by the identity matrix as the preconditioner. However, this is slightly slower than using the direct linear solvers. We also tested the approach used by Grue et al. [18] who first inverted the last equation of (74) by Gaussian elimination, expressed $\mathcal{T}_b$ as a function of $\mathcal{N}$ and $\mathcal{U}$, then solved the other two equations by iterative solvers. We found that this is also slower than directly solving these linear equations. After substituting $\mathcal{T}_b$, the original coefficient of $\mathcal{N}$ and $\mathcal{U}$ is significantly modified, finally resulting in non-clustered eigenvalues of the new coefficient matrix. Note that there exist other efficient iterative methods, such as the Ewald summation method and its relatives [3–5,8,21]. These methods play a significant role in three-dimensional simulations of water waves.

### 5.2. Time integration

To perform time integration, we transform Eqs. (24), (30), (34), (35) and (41) into Fourier space and integrate them using Runge–Kutta methods. It is found that the aliasing error is better controlled in Fourier

space compared to integrating these equations in physical space. The small-scale decomposition method developed by [16], which is essentially a integrating-factor technique, is particularly useful for stiff systems. By numerical tests, we find that it is equally efficient to direct time integration. Most computations are performed using the standard Runge–Kutta 4th-order method (RK4). In addition, the adaptive Runge–Kutta–Fehlberg method (RKF45) which automatically updates the time step via embedded fourth-order and fifth-order time schemes are also used to confirm some of the results. This is more efficient compared with the constant-step Runge–Kutta method. In principle, higher-order time-marching algorithms can be used. However, we find the RK4 and the RKF45 schemes balance well accuracy and efficiency.

### 5.3. Numerical filter

In some simulations, we apply the following two numerical filters to control the aliasing error.

1. The 36th-order Fourier filter invented by Hou and Li [22]

$$f(k) = \mathrm{e}^{-36(k/k_{max})^{36}}, \tag{77}$$

where $k_{max}$ denotes the Nyquist wave number.
2. The 15th-order smoothing polynomial invented by Dold [6].

### 5.4. Numerical accuracy

To measure the numerical accuracy, we define the relative error of energy $E_r(t)$

$$E_r(t) = \frac{|E(t) - E(0)|}{E(0)}, \tag{78}$$

where $E(t)$ is the energy calculated in one period

$$E(t) = \frac{1}{2}\iint_{-h_1<y<\eta(x)} |\nabla\phi_1|^2 \,\mathrm{d}x\mathrm{d}y + \frac{R}{2}\iint_{\eta(x)<y<h_2} |\nabla\phi_2|^2 \,\mathrm{d}x\mathrm{d}y + \frac{1-R}{2}\int_0^{2\pi/k} \eta^2 \,\mathrm{d}x + \int_0^{2\pi/k} \left(\sqrt{1+\eta_x^2} - 1\right) \mathrm{d}x. \tag{79}$$

Using the divergence theorem, $E(t)$ can be simplified to integrals evaluated on the interface

$$E(t) = \frac{S}{2}\int_0^1 \overline{\varphi}\mathcal{N}\,\mathrm{d}l + \frac{(1-R)S}{2}\int_0^1 \eta^2\cos\theta\,\mathrm{d}l + S\int_0^1 (1-\cos\theta)\,\mathrm{d}l. \tag{80}$$

When surface tension is absent, we drop the last term.

In the numerical tests for travelling waves, another useful estimation of numerical accuracy is the profile differences on the collocation points (function $\gamma(t)$ is then chosen according to Case II). We define

$$\Delta\eta = \eta(l,t) - \eta(l,0), \tag{81}$$

to measures the difference of $\eta$ at the same collocation points after an integer number of temporal periods.

## 6. Numerical tests

In this section, we present six numerical tests including interfacial waves and surface waves. In the first four experiments, we nondimensionalize the system by using scalings (10). In the last two experiments, scalings (11) are used.

### 6.1. Travelling waves

We first consider the propagation of a periodic interfacial gravity-capillary wave as shown in Fig. 4. The initial condition is an exact

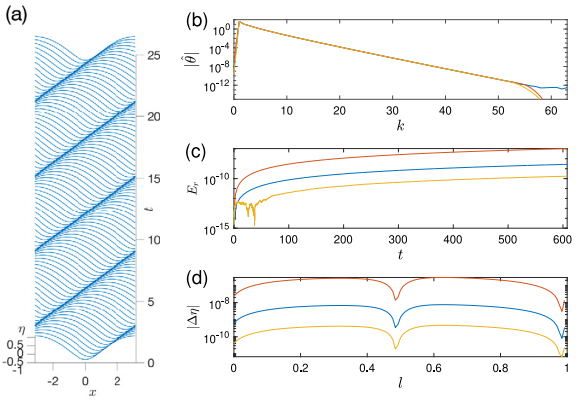


**Fig. 4.** Simulation of a periodic travelling interfacial gravity-capillary wave with $R = 0.5$, $k = 1$, $h_1 = h_2 = \infty$, and $H = 1.4$. (a) Wave profiles in the first four temporal periods. (b) Spectrum of $\theta$ at $t = 100T_0$. Blue: $\Delta t = T_0/5000$; red: $\Delta t = T_0/2000$; yellow: $\Delta t = T_0/10000$. The Fourier filter is turned off for the blue curve and turned on for the red and yellow curves. (c) Energy error $E_r$. (d) $|\Delta\eta|$ at $t = 100T_0$.

travelling-wave solution calculated using Newton's method [23]. The density ratio $R = 0.5$, wave number $k = 1$, water depths $h_1 = h_2 = \infty$, and crest-to-trough height $H = 1.4$. We let $N = 128$ and run the simulations for $100T_0$, where $T_0 \approx 6.077$ is the temporal period. In Fig. 4(a), we show the wave profiles in the first four temporal periods which exhibit a perfect travelling-wave form. In Fig. 4(b), we display the spectrum of $\theta$ at $t = 100T_0$. The blue curve is the result with time step $\Delta t = T_0/5000$. No filter is applied and no obvious numerical aliasing is observed. By comparison, the red and yellow curves are calculated with $\Delta t = T_0/2000$ and $T_0/10000$ with the Fourier filter (77) turned on. The differences of the three spectrum only appear in the last one eighth wave components whose Fourier coefficients have amplitude around $O(10^{-12})$. Therefore, we expect that the Fourier filter removes little energy from the system. This is confirmed by the relative error of energy $E_r$ plotted in Fig. 4(c). It clearly shows the numerical error decreases when $\Delta t$ gradually becomes small. In addition, we performed the simulation with $\Delta t = T_0/5000$ when the Fourier filter (77) is used. It turns out the energy curve perfectly overlaps the blue one, i.e., the result obtained with the same $\Delta t$ but no filter. The same conclusion can be drawn by comparing the profile difference at $t = 0$ and $100T_0$, which is plotted in Fig. 4(d) in a log-scale. In Fig. 4(c) and (d), the explanation of the different curves is same as those in Fig. 4(b).

The second numerical test is the propagation of a depression interfacial gravity-capillary solitary wave in deep water. The initial condition is an exact travelling-wave solution calculated using Newton's method in a long periodic domain where $x \in [-90, 90]$. The density ratio $R = 0.2$, water depths $h_1 = h_2 = \infty$, and maximum amplitude $H = \max(|\eta(l,0)|) = 0.5$. We choose $N = 2048$, and $\Delta t = 5\times10^{-3}$ and $2.5\times10^{-3}$. The Fourier filter (77) is turned on during the simulation. Fig. 5(a)–(c) shows the time evolution of the interface at $t = 0, 37.5$ and 75. A perfect travelling wave is observed. At $t = 1000$, we reverse time and perform a backward simulation down to the initial time $t = 0$. In Fig. 5(d), we plot the relative error of energy $E_r$ for the two time steps, showing that $E_r$ can be well controlled by decreasing $\Delta t$. In Fig. 5(e), we compare the final interface after time reversing and the initial interface by plotting $\Delta\eta(l, 2000)$. The two interfaces agree perfectly with numerical error less than $4\times10^{-8}$ ($\Delta t = 5\times10^{-3}$) and $7\times10^{-10}$ ($\Delta t = 2.5\times10^{-3}$).

### 6.2. Head-on collision of solitary waves

The third numerical experiment is a head-on collision of two interfacial gravity-capillary solitary waves as shown in Figs. 6 and 7.

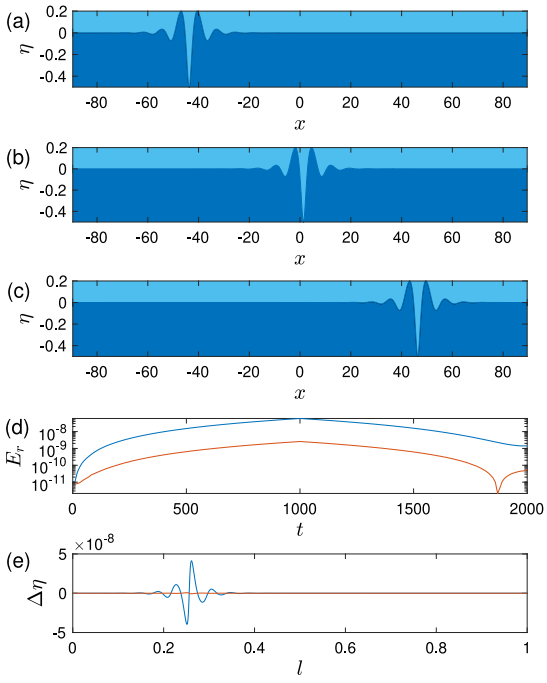


**Fig. 5.** A travelling interfacial gravity-capillary solitary wave of depression type. Wave amplitude $H = 0.5$, density ratio $R = 0.2$ and water depth $h_1 = h_2 = \infty$. Calculations are performed with $N = 2048$ and $\Delta t = 0.005$. (a)–(c) $t = 0, 37.5$ and 75. (d) Relative error of energy $E_r$. (e) $\Delta\eta$ at $t = 2000$. Blue and red curves correspond to $\Delta t = 5 \times 10^{-3}$ and $2.5 \times 10^{-3}$.

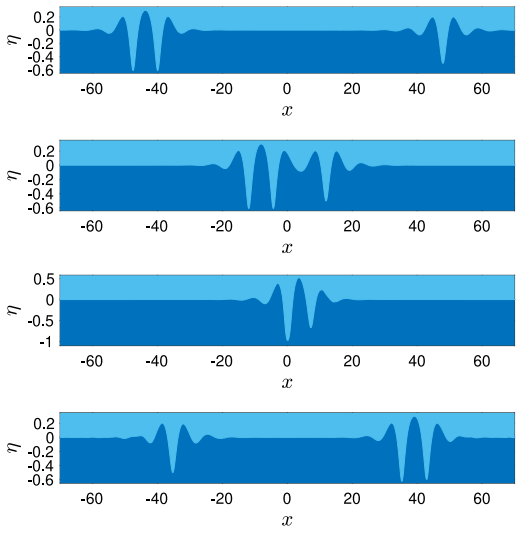


**Fig. 6.** A head-on collision of two interfacial gravity-capillary solitary waves of depression type ($H = 0.5$) and elevation type ($H = 0.3$). Density ratio $R = 0.2$, and water depth $h_1 = h_2 = \infty$. Calculations are performed with $N = 2048$ and $\Delta t = 0.005$. $t = 0, 30, 40$ and 70 from the top figure to the bottom figure.

It is well-known that for surface gravity-capillary solitary waves in deep water, the depression solutions are linearly stable. On the other hand, the elevation solutions are linearly unstable except those between the first and second energy turning points on the bifurcation branch. Both linear-stability analysis and nonlinear simulation yield the same conclusion [13,24]. However, for interfacial gravity-capillary solitary waves, there is no nonlinear simulation based on Euler equations to

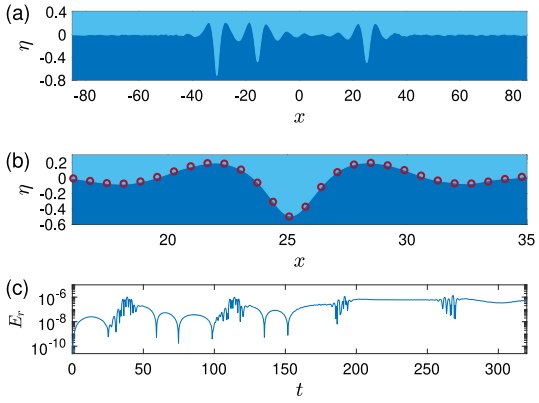


**Fig. 7.** (a) Wave profile at $t = 320$ after four continuous head-on collisions. (b) Local profiles of the depression solitary wave. Curve: $t = 320$; circles: $t = 0$. (c) Relative error of energy.

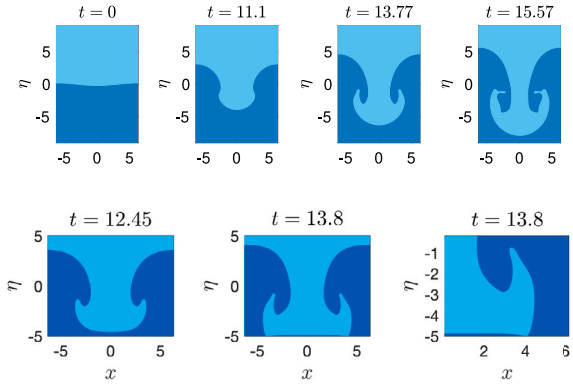


**Fig. 8.** Simulations of the R–T instability. Top: $R = 2$, $h_1 = h_2 = \infty$, $k = 0.5$. Bottom: $R = 2$, $h_1 = h_2 = 5$, $k = 0.5$.

the best of our knowledge. To check their stability, we perform a long-term simulation of head-on collision in a long periodic domain where $x \in [-90, 90]$. The numerical settings are the same as those in the last numerical test. We choose the depression solitary wave plotted in Fig. 5, as well as an elevation solitary wave with maximum amplitude $H = \max(|\eta(l, 0)|) \approx 0.6$. Initially, the elevation and depression waves are separated far from each other and travel to the right and left, respectively. Fig. 6 displays four profiles at $t = 0, 30, 40$ and 70 during the first head-on collision. After that, both waves exhibit a little asymmetry and radiate small ripples travelling to their front side. Due to the periodic boundary condition, the two solitary waves can keep colliding in the computation domain. Fig. 7(a) exhibits the wave profiles at $t = 320$ after four continuous head-on collisions. The depression solitary wave still maintains its initial profile. This can be clearly seen in Fig. 7(b) where we plot the profile of the depression solitary wave at $t = 0$ (red circles) by horizontally shifting it to match the profile at $t = 320$. The elevation solitary wave, on the other hand, gradually splits into two depression waves. This means the depression solitary waves in deep water are likely to be stable with respect to two-dimensional disturbances, while the elevation waves are likely to be unstable. In Fig. 7(c), we plot the relative error of energy $E_r$. It is well controlled and less than $10^{-6}$ in the simulation.

### 6.3. R–T instability

In the dispersion relation (16), when density ratio $R > 1$, $\omega^2$ becomes negative if $k < \sqrt{R-1}$, yielding the R–T instability. In our

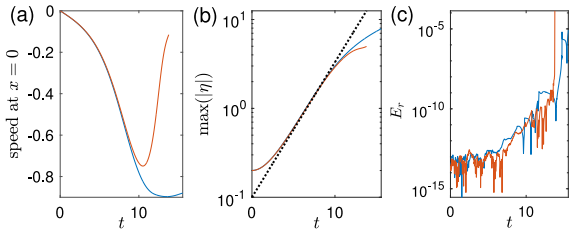


**Fig. 9.** Results of the R–T instability in deep-water case (blue) and finite-depth case (red). (a) Speed of interface at $x = 0$. (b) $\max(|\eta|)$ versus $t$. The dotted line represent $0.1e^{0.35t}$ (c) Relative energy error.

fourth numerical experiment, we set $R = 2$ and $k = 0.5$ and apply the following initial conditions

$$\theta(l, 0) = -0.1\sin(2\pi l), \qquad \overline{\varphi}(l, 0) = 0.$$

We consider two different scenarios: $h_1 = h_2 = \infty$ (deep-water case) and $h_1 = h_2 = 5$ (finite-depth case). Initially, computations are performed with $N = 128$ and $\Delta t = 0.001$. The Fourier filter (77) is used. When the number of Fourier components is not large enough to maintain the numerical accuracy, we double $N$ and use Fourier interpolation. In the final computation, $N = 2048$. In Fig. 8, we show the interfaces at different times. The top figures correspond to the deep-water case, while the bottom figures are the finite-depth case. The heavier fluid quickly falls into the lighter one and forms round interfaces at the crest and trough. The profiles then become overhanging and generate two counter-rotating fingers. The results in two scenarios are nearly the same when $t < 10$. This can be seen from Fig. 9(a) and (b) where we show the speed of interface at $x = 0$, and $\max(|\eta|)$. The blue and red curves correspond to the deep-water and finite-depth case, and are almost indistinguishable when $t < 10$. The dotted line in (b) represents $0.1\exp(0.35t)$, according to the linear theory. It agrees well with nonlinear simulations until $t > 10$. The interface then keeps falling at an almost constant speed in the deep-water case. The fingers keeps rolling up and pinching. At the final state, two symmetric closed bubbles are nearly formed when the interface becomes almost self-intersecting. On the other hand, the interface "feels" the existence of bottom wall in the finite-depth case and starts slowing down its falling speed after $t = 10.6$. The interface gradually becomes flat at the crest and trough, and ultimately develops two symmetric corners which almost touch the bottom wall, leaving a slender fluid bubble between the interface and the bottom wall. In Fig. 9(c), we show the energy error $E_r$ of the two simulations. Same results are obtained using the RKF45.

### 6.4. Breaking of surface waves

In the fifth numerical experiment, we exhibit a simulation of surface-wave breaking. The initial condition is an exact travelling Stokes wave calculated using Newton's method. To trigger wave breaking, different strategies have been invented: Longuet-Higgins and Cokelet [1] applied an artificial pressure on the surface; Dold [6] elevated the bottom wall suddenly at $t = 0$. Here what we apply is amplifying wave profile by a factor $\mu$ initially. This is implemented by performing the following operations

$$\theta(l) \to \theta(l), \quad \overline{\varphi}(l) \to \overline{\varphi}(l), \quad S \to \mu S, \quad x_0 \to \mu x_0, \quad k \to k/\mu.$$

Instead of using the Fourier filter (77), the 15th-order smoothing polynomial [6] turns out to be more robust. In Fig. 10, a Stokes wave having unit water depth, crest-to-trough amplitude $H = 0.6$ and wave number $k = 1$ is amplified by factor $\mu = 3$ and set to be the initial condition. We choose $\Delta t = 5 \times 10^{-4}$ with different values of $N$. At the initial stage, the gravitational energy $E_p$ is transferred to the kinematic energy

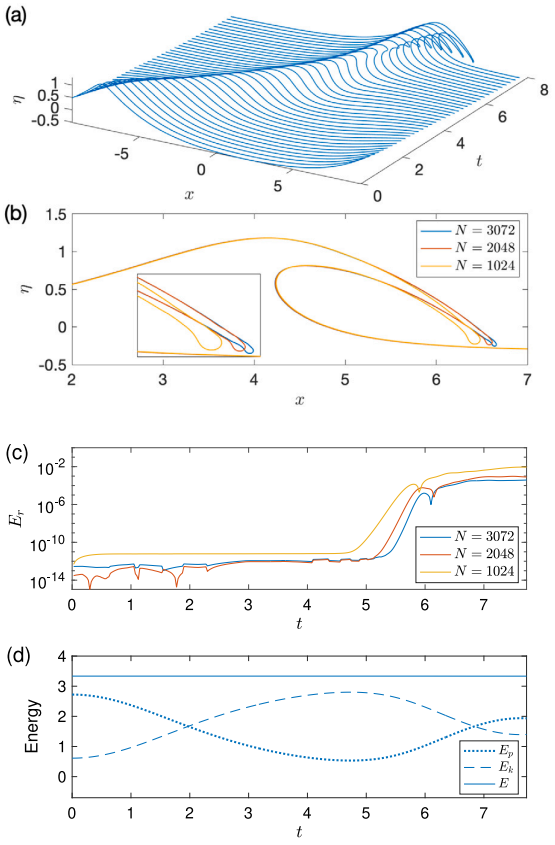


**Fig. 10.** Simulation of a breaking surface gravity wave. (a) Wave profiles at different time. (b) Wave profiles at $t = 7.725$ with $N = 1024, 2048$ and 3072. (c) Relative error of total energy with $N = 1024, 2048$ and 3072. (d) Kinetic energy, gravitional energy and total energy with $N = 3072$.

$E_k$, resulting in an accelerating moving front. At $t \approx 5.375$, the wave develops a vertical tangent and then becomes overhanging. A plunging breaker appears and becomes sharp at its tip. At $t = 7.725$, the wave becomes almost self-touching and encloses an air bubble on its front face. The whole process of breaking is shown in Fig. 10(a). The nipple of the breaker has a locally round shape and tiny wiggles, probably resulting from numerical oscillations due to the drastic increase of curvature. Higher resolutions are necessary to guarantee the numerical accuracy. A comparison of the wave profile at $t = 7.725$ with $N = 1024, 2048$ and 3072 is plotted on the bottom of Fig. 10(b). The total energy is shown to be a constant between 3.334 and 3.335. At $t \approx 4.75$, the kinetic energy $E_k$ and gravitational potential energy $E_p$ reach their extremums. Shortly after that, the wave becomes overturned and the relative energy error $E_r$ increases rapidly, as shown in Fig. 10(d). When $N = 1024, 2048$ and 3072, the upper bounds of $E_r$ are and $10^{-2}, 10^{-3}$ and $3\times10^{-4}$ respectively, exhibiting gradually convergent solutions. We also apply the RKF45 with $N = 3072$ and obtain the same result.

### 6.5. Surface waves over bottom topography

In our final numerical test, we present simulations of surface gravity waves propagating over bottom topography. In Fig. 11, a surface gravity solitary-wave solution with a maximum amplitude of 0.15 is selected as the initial condition. Two types of symmetric topographies are considered: (1) a table-top profile with a maximum amplitude of 0.5 at $x = 0$; and (2) an oscillating profile with a wavelength of 12.6, modulated by a Gaussian envelope with a maximum amplitude of 0.3. In

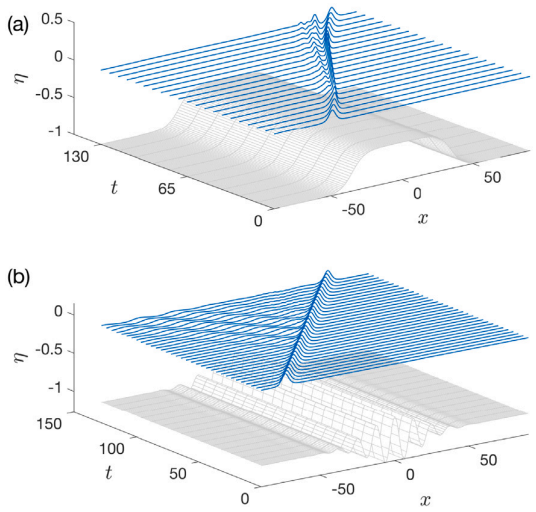


**Fig. 11.** Simulations of surface gravity solitary wave passing over bottom topography. (a) Table-top bottom. (b) Locally oscillating bottom.

these simulations, we set $\Delta t = 0.01$, with $N = 2048$ for the first scenario and $N = 1024$ for the second. No numerical filter is applied. For the table-top bottom profile shown in Fig. 11(a), the solitary wave becomes taller and steeper as it enters the depth-decreasing region. Distortion gradually appears on its rear side, generating a smaller wave behind it. As the solitary wave reaches the shallow-water region, where the depth is 0.5, it accelerates to a nearly constant speed and splits into a taller leading wave with an amplitude of approximately 0.25, followed by a smaller trailing wave. Upon reaching the depth-increasing region, each of these waves again becomes distorted, radiating smaller waves from their trailing edges. Only very small reflection waves are observed, with amplitude around $10^{-3}$. When the solitary wave propagates over the oscillating bottom, shown in Fig. 11(b), a train of reflected waves forms on the trailing edge, with a wavelength twice that of the bottom oscillations. This is exactly the Bragg resonance [25]. The maximum crest-to-trough amplitude of these reflected waves is approximately 0.025. Additionally, small-amplitude waves, matching the wavelength of the bottom oscillations, are generated initially right above the oscillations and then spread in both directions. The amplitude of the solitary waves oscillates between 0.144 and 0.156, eventually stabilizing at 0.146. After passing over the bottom topography, a third type of small-amplitude waves with a typical wave length of 4 is observed travelling to the right. For both simulations, the energy error $E_r$ is less than $10^{-8}$.

## 7. Conclusions and perspectives

In this paper, we developed a boundary-integral algorithm for two-dimensional, unsteady, nonlinear interfacial waves. The algorithm uses the tangent angle $\theta$ and the density-weighted velocity potential $\overline{\varphi}$ as primary unknowns, with arclength $s$ parameterizing the interface. This approach enables simulations of overhanging interfaces in two-layer inviscid flows. To solve the Laplace's equation, we used Cauchy's integral formula. It transforms the problem into a Fredholm integral equation of the second kind, which can be solved efficiently and accurately by either an iterative solver or a direct linear solver. The numerical scheme is based on an Eulerian or mixed Eulerian–Lagrangian description, ensuring a uniform distribution of collocation points and maintaining high physical resolution. Compared to the vortex-sheet method which is primarily restricted to flows without boundaries, our method offers significant flexibility, allowing to handle waves over deep water, finite-depth water, or complex bottom topography.

We demonstrated that our algorithm possesses both numerical efficiency and broad applicability through six numerical experiments. The numerical scheme is neutrally stable and conserves energy with superior accuracy. No significant numerical stiffness is observed, thus allowing for simulations over very long time periods. In particular, we conducted simulations of the travelling and head-on collision of interfacial gravity-capillary solitary waves, exhibiting their stability. To the best of our knowledge, this is likely the first simulation of these waves based on the full Euler equations. We also simulated the Rayleigh–Taylor instability in both unbounded and bounded regions to illustrate the interaction between the interface and solid boundaries. Additionally, the numerical experiments also included surface gravity waves, including their breaking and interaction with bottom topography. In all numerical tests, the energy error was calculated and found to be well-controlled.

Our numerical algorithm can easily be extended to more complex physical scenarios, including mode-2 internal waves in three-layer flows, interfacial waves in electric fields, and interfacial waves interacting with a constant vorticity or a time-dependent topography. It is presently confined to periodic waves in two dimensions, thus necessitating further exploration to overcome these limitations. Numerical schemes based on the Chebyshev spectral method show promise for integration into the $\theta - s$ formulation to simulate non-periodic waves with great numerical accuracy. Green's function has already been employed for three-dimensional nonlinear waves in specific scenarios [3,4,21,26]. Nevertheless, the development of a three-dimensional boundary-integral algorithm that effectively balances accuracy, efficiency, and applicability remains a significant challenge for future research.

## CRediT authorship contribution statement

**Xin Guan:** Writing – original draft, Software, Methodology, Conceptualization. **Jean-Marc Vanden-Broeck:** Writing – review & editing.

## Declaration of competing interest

The authors declare that they have no known competing financial interests or personal relationships that could have appeared to influence the work reported in this paper.

## Appendix. Derivation of Eq. (41)

The dimensionless Bernoulli equations on the interface for the lower and upper layers are

$$\phi_{1,t} + \frac{1}{2}(\mathcal{T}_1^2 + \mathcal{N}^2) + \eta + p_1 = 0, \tag{A.1}$$

$$R\phi_{2,t} + \frac{R}{2}(\mathcal{T}_2^2 + \mathcal{N}^2) + R\eta + p_2 = 0. \tag{A.2}$$

We introduce

$$\varphi_1(l,t) = \phi_1\big(x(l,t), \eta(l,t), t\big), \tag{A.3}$$

$$\varphi_2(l,t) = \phi_2\big(x(l,t), \eta(l,t), t\big), \tag{A.4}$$

then

$$\begin{aligned}\frac{D\varphi_1}{Dt} &= \varphi_{1,t} + \varphi_{1,l}\frac{D}{Dt}\left(\frac{s}{S}\right)\\ &= \phi_{1,t} + \boldsymbol{u_1}\cdot\nabla\phi_1 = \phi_{1,t} + \mathcal{T}_1^2 + \mathcal{N}^2,\end{aligned} \tag{A.5}$$

so we have

$$\phi_{1,t} = \varphi_{1,t} + \varphi_{1,l}\frac{D}{Dt}\left(\frac{s}{S}\right) - \mathcal{T}_1^2 - \mathcal{N}^2. \tag{A.6}$$

Using Eq. (26), it becomes

$$\phi_{1,t} = \varphi_{1,t} + \mathcal{T}_1\frac{Ds}{Dt} + \mathcal{T}_1 l\int_0^1 \theta_l \mathcal{N}\,\mathrm{d}l - \mathcal{T}_1^2 - \mathcal{N}^2. \tag{A.7}$$

Similarly, we have

$$\phi_{2,t} = \varphi_{2,t} + \mathcal{T}_2 \frac{Ds'}{Dt} + \mathcal{T}_2 I \int_0^1 \theta_l \mathcal{N} \, \mathrm{d}l - \mathcal{T}_2^2 - \mathcal{N}^2. \tag{A.8}$$

Note that $Ds'/Dt$ is the material derivative fixed on the upper fluid particles, and has following form

$$\frac{Ds'}{Dt} = \int_0^l \left(\mathcal{T}_2 - \theta_l \mathcal{N}\right) \mathrm{d}l + \gamma(t) + \mathcal{T}_2(0,t) - \mathcal{T}_1(0,t). \tag{A.9}$$

Using Eq. (27), we obtain

$$\phi_{1,t} = \varphi_{1,t} - \mathcal{T}_1(0,t)\mathcal{T}_1 - \mathcal{T}_1 \int_0^l P\left(\theta_l \mathcal{N}\right) \mathrm{d}l - \mathcal{N}^2, \tag{A.10}$$

$$\phi_{2,t} = \varphi_{2,t} - \mathcal{T}_1(0,t)\mathcal{T}_2 - \mathcal{T}_2 \int_0^l P\left(\theta_l \mathcal{N}\right) \mathrm{d}l - \mathcal{N}^2, \tag{A.11}$$

where $P$ is the zero-mean operator defined in (31). Substituting into (A.1) and (A.2) and using the Young–Laplace equation (surface tension coefficient has been normalized to 1)

$$p_2 - p_1 = \theta_l / S, \tag{A.12}$$

we ultimately obtain

$$\begin{aligned}\overline{\varphi}_t = \mathcal{T}_1(0,t)\overline{\mathcal{T}} + \frac{(1-R)\mathcal{N}^2}{2} - \frac{\mathcal{T}_1^2 - R\mathcal{T}_2^2}{2} - (1-R)\eta \\ + \frac{\theta_l}{S} + \overline{\mathcal{T}} \int_0^l P\left(\theta_l \mathcal{N}\right) \mathrm{d}l - \overline{\mathcal{T}}\gamma.\end{aligned} \tag{A.13}$$

## Data availability

Data will be made available on request.

## References


[1] Longuet-Higgins MS, Cokelet ED. The deformation of steep surface waves on water-I. A numerical method of computation. Proc R. Soc Lond A 1976;350(1660):1–26.

[2] Yang Y. The initial value problem of a rising bubble in a two-dimensional vertical channel. Phys Fluids 1992;4(5):913–20.

[3] Fructus D, Clamond D, Grue J, Kristiansen Ø. An efficient model for three-dimensional surface wave simulations: Part I: Free space problems. J Comput Phys 2005;205(2):665–85.

[4] Clamond D, Fructus D, Grue J, Kristiansen Ø. An efficient model for three-dimensional surface wave simulations. Part II: Generation and absorption. J Comput Phys 2005;205(2):686–705.

[5] Fructus D, Grue J. An explicit method for the nonlinear interaction between water waves and variable and moving bottom topography. J Comput Phys 2007;222(2):720–39.

[6] Dold JW. An efficient surface-integral algorithm applied to unsteady gravity waves. J Comput Phys 1992;103(1):90–115.

[7] Schultz WW, Huh J, Griffin OM. Potential energy in steep and breaking waves. J Fluid Mech 1994;278:201–28.

[8] Clamond D, Grue J. A fast method for fully nonlinear water-wave computations. J Fluid Mech 2001;447:337–55.

[9] Ambrose DM, Camassa R, Marzuola JL, McLaughlin RM, Robinson Q, Wilkening J. Numerical algorithms for water waves with background flow over obstacles and topography. Adv Comput Math 2022;48(4):46.

[10] Baker GR, Meiron DI, Orszag SA. Generalized vortex methods for free-surface flow problems. J Fluid Mech 1982;123:477–501.

[11] Murashige S, Choi W. A numerical study on parasitic capillary waves using unsteady conformal mapping. J Comput Phys 2017;328:234–57.

[12] Craig W, Sulem C. Numerical simulation of gravity waves. J Comput Phys 1993;108(1):73–83.

[13] Wang Z. Stability and dynamics of two-dimensional fully nonlinear gravity–capillary solitary waves in deep water. J Fluid Mech 2016;809:530–52.

[14] Baker GR, Meiron DI, Orszag SA. Vortex simulations of the Rayleigh–Taylor instability. Phys Fluids 1980;23(8):1485–90.

[15] Pullin DI. Numerical studies of surface-tension effects in nonlinear Kelvin–Helmholtz and Rayleigh–Taylor instability. J Fluid Mech 1982;119:507–32.

[16] Hou TY, Lowengrub JS, Shelley MJ. Removing the stiffness from interfacial flows with surface tension. J Comput Phys 1994;114(2):312–38.

[17] Hou TY, Lowengrub JS, Shelley MJ. Boundary integral methods for multicomponent fluids and multiphase materials. J Comput Phys 2001;169(2):302–62.

[18] Grue J, Friis HA, Palm E, Rusaas PO. A method for computing unsteady fully nonlinear interfacial waves. J Fluid Mech 1997;351:223–52.

[19] Rangel RH, Sirignano WA. Nonlinear growth of Kelvin–Helmholtz instability: Effect of surface tension and density ratio. Phys Fluids 1988;31(7):1845–55.

[20] Baker GR, Nachbin A. Stable methods for vortex sheet motion in the presence of surface tension. SIAM J Sci Comput 1998;19(5):1737–66.

[21] Ambrose DM, Siegel M, Tlupova S. A small-scale decomposition for 3D boundary integral computations with surface tension. J Comput Phys 2013;247:168–91.

[22] Hou TY, Li R. Computing nearly singular solutions using pseudo-spectral methods. J Comput Phys 2007;226(1):379–97.

[23] Guan X, Vanden-Broeck JM, Wang Z. New solutions for interfacial capillary waves of permanent form. J Fluid Mech 2022;951:A43.

[24] Calvo DC, Akylas TR. Stability of steep gravity–capillary solitary waves in deep water. J Fluid Mech 2002;452:123–43.

[25] Alam MR, Liu Y, Yue DKP. Bragg resonance of waves in a two-layer fluid propagating over bottom ripples. Part I. Perturbation analysis. J Fluid Mech 2009;624:191–224.

[26] Grilli ST, Guyenne P, Dias F. A fully non-linear model for three-dimensional overturning waves over an arbitrary bottom. Internat J Numer Methods Fluids 2001;35(7):829–67.